nature physics

Article

https://doi.org/10.1038/s41567-025-03146-7

Transport evidence for chiral surface states from three-dimensional Landau bands

Received: 14 December 2024

Accepted: 21 November 2025

Published online: 16 January 2026

Check for updates

Junho Seo [1] ✉, Chunyu Mark Guo [1], Carsten Putzke [1], Xiangwei Huang [2,3], Berit H. Goodge [4], Yip Chun Wong [5], Mark H. Fischer [5] ✉, Titus Neupert [5] ✉ & Philip J. W. Moll [1] ✉

Strong magnetic fields applied to metals confine electrons into Landau orbits, except at the boundaries at which frequent surface collisions disrupt their cyclotron motion. In two-dimensional systems, these boundary states form dissipationless chiral edge channels in the quantum Hall regime. By contrast, the quantum limit of three-dimensional (3D) metals is traditionally thought to differ fundamentally and instead contains gapless Landau bands, lacking quantized Hall conductance or dissipationless transport. Here we demonstrate enhanced surface conduction in the quantum limit of the 3D semimetal bismuth, characterized by the counterintuitive increase in conductivity as material is removed by micropatterning. The conductance of the 3D chiral boundary states—3D analogues of quantum Hall states in two dimensions—naturally accounts for this behaviour and for the highly non-local transport observed in micrometre-sized crystalline bismuth structures. These findings introduce an approach for engineering and exploiting chiral conduction on the surfaces of 3D materials, offering a design space for geometries beyond the simple one-dimensional boundary modes of two-dimensional systems.

The quantum Hall effect (QHE) is a remarkable manifestation of topology in matter, accompanied by non-trivial observables such as dissipationless transport and a Hall effect quantized to e^2/h irrespective of the material's parameters[1–3]. The motion of electrons in two dimensions is semiclassically constrained by perpendicular magnetic fields to cyclotron orbits, which, on quantization, leads to discrete, flat energy bands—the Landau levels. The bulk electronic spectrum is, thus, gapped, whereas the boundary of the system hosts gapless chiral edge states that arise from the interrupted cyclotron motion skipping along the edge. The topological invariant characterizing this system is the number of filled Landau levels, which, in turn, determines the number of chiral edge channels (Fig. 1a). By contrast, in three-dimensional (3D) systems, electrons may move along the magnetic field direction without being affected by the Lorentz force. The electron momentum k_z along the field (commonly denoted as the z direction), thus, serves as an additional degree of freedom, which, in a semiclassical picture, leads to the well-known helical motion of free electrons along the magnetic field direction. In the quantum picture, Landau levels are now macroscopically degenerate one-dimensional dispersive modes, with k_z being the appropriate quantum number. For a metallic band structure, in other words, a gapless band structure in the absence of a magnetic field, one generically obtains partially occupied Landau bands with a well-defined Fermi momentum in a magnetic field. Hence, the bulk remains gapless even with a magnetic field, in contrast to the two-dimensional (2D) case. This leaves no room for any strictly quantized, topological observables and implies a natural hybridization of any surface states with the bulk states.

[1]Max Planck Institute for the Structure and Dynamics of Matter, Hamburg, Germany. [2]Laboratory of Quantum Materials (QMAT), Institute of Materials (IMX), École Polytechnique Fédérale de Lausanne (EPFL), Lausanne, Switzerland. [3]Marine Science and Technology Domain, Beijing Institute of Technology, Zhuhai, China. [4]Max Planck Institute for Chemical Physics of Solids, Dresden, Germany. [5]Department of Physics, University of Zürich, Zürich, Switzerland. ✉e-mail: junho.seo@mpsd.mpg.de; mark.fischer@uzh.ch; titus.neupert@uzh.ch; philip.moll@mpsd.mpg.de

https://doi.org/10.1038/s41567-025-03146-7

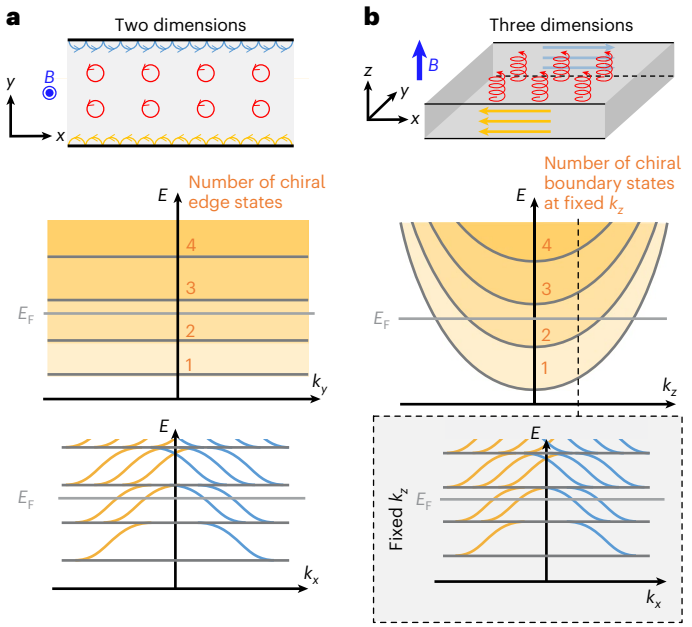

Fig. 1 | Magnetic-field-induced chiral boundary states of the 3D band structure in the quantum limit. a, Schematic of a 2D quantum Hall system. Under strong magnetic fields, electrons are semiclassically constrained to cyclotron orbits, and their energy levels are quantized into discrete Landau levels (grey lines). Along the boundary of the system, electrons are confined to the chiral edge states (orange and blue), which propagate in one direction without backscattering. The number of chiral edge states is determined by the number of filled Landau levels. **b**, Schematic of a 3D system under strong magnetic fields. Here electron motion in the plane perpendicular to the magnetic field is confined to a cyclotron orbit, whereas it can propagate along the magnetic field direction (z), forming a helical trajectory in the semiclassical picture. Hence, a 3D system has one-dimensional dispersive Landau bands (grey lines) in the k_z momentum space. For every k_z lying between momenta at which the lowest Landau level crosses the Fermi level, chiral boundary states (orange and blue) exist in the k_x momentum space at fixed k_z. The number of chiral boundary modes is determined by the number of occupied (k_z-dispersive) Landau levels.

Yet, akin to the 2D case, 3D semiclassical electron trajectories at the surfaces parallel to the magnetic field cannot complete cyclotronic motion and yield skipping orbits. These states and their transport properties are the main focus of this work. Semiclassically, skipping orbits can contribute to ballistic or diffusive transport depending on the momentum conservation rules at the scattering event, often subsumed into a specularity coefficient. Regardless of specularity, however, these modes are strictly chiral as the sign of the Lorentz force yields a definite sense of circulation and, therefore, of dominant surface propagation. In a quantum mechanical picture, the modes form a 3D analogue of the chiral edge states characterized by the two momenta preserved by the surface. For concreteness, we label the momentum along the magnetic field k_z and the one surface momentum k_x, in analogy to 2D QHE systems. Such a 3D system retains close links to the quantum Hall system, which is most evident for the $k_z = 0$ state that is equivalent to the 2D QHE edge states embedded in three dimensions. Even for each finite value of k_z, the system realizes a 2D quantum Hall state with a number of chiral boundary modes determined by the number of occupied (k_z-dispersive) Landau levels (Fig. 1b). These are generic surface states that appear on surfaces parallel to the magnetic field in 3D Landau bands, in contrast to the gapless Dirac surface states found in 3D topological insulators[4]. On the other hand, these chiral boundary states are comparable with the chiral states resulting from a Fermi arc in Weyl semimetals under a magnetic field[5]. The main difference is that the gap of the former is given by the cyclotron gap between the Landau bands, whereas for the latter, the gap is the band energy scale separating the Weyl points (for example, spin–orbit coupling). The transport contribution of such chiral boundary states is also similar to that of Fermi arc states in a Weyl semimetal as they carry a non-quantized Hall current and a longitudinal current with long lifetimes[6–8]. The latter is a result of the substantially reduced phase space for backward scattering, which requires either large momentum transfer to other surface states or scattering into bulk states.

The fate of the QHE, particularly the question of how quantization is restored in three dimensions, is a long-standing topic[5,9–19], which recently sparked intense research activities due to the discovery of approximately quantized Hall plateaus in low-carrier-density 3D systems such as $ZrTe_5$ and Cd_3As_2 (refs. 14–19). Quantized Hall and zero longitudinal resistance in these special cases could arise from finite gaps due to, for instance, charge density instabilities in Landau bands[14–16]. Of particular interest is the quantum limit—a situation in which charge carriers only occupy the lowest Landau level.

In contrast to these bulk characterizations, the chiral boundary states in the quantum limit of 3D metals have not received similar attention. Importantly, the design space for boundaries of 3D systems is much larger than in 2D systems. In momentum space, the degrees of freedom live on a one-dimensional Fermi surface compared with zero-dimensional Fermi points of a chiral edge mode. Beyond these degrees of freedom, the 2D surface of a 3D system can be engineered into complex shapes, thereby tuning and controlling the participation of chiral surface modes in transport.

Bismuth has been a pivotal semimetal in the study of quantum phenomena due to its low carrier density and highly anisotropic Fermi surface[20,21]. Although its classification as a higher-order topological insulator in the absence of a magnetic field has received attention[22–25], the application of even a moderate magnetic field can drive all the electron pockets at the L points or the hole pocket at the T point into the quantum limit depending on the field orientation[21]. Hereafter, with the quantum limit, we refer to the quantum limit of electron pockets. The field orientation/magnitude in this work cannot drive the hole pocket into this limit[21]. In our work, we cut microscopic crystalline conductors of varying 3D shapes from macroscopic bismuth crystals using focused-ion-beam (FIB) machining. These micrometre-sized structures are sufficiently large to be in the bulk limit without finite-size quantization effects, yet sufficiently small to show significant transport from chiral boundary states. Most strikingly, cutting trenches or grooves into the surface substantially increases the sample conductance under quantum-limit magnetic fields applied parallel to the sample's surface. This is in contrast to the usual expectation of decreasing conductance when material and, hence, conduction channels are removed from a conductor, a common scaling trend indeed observed in the bismuth structures at zero field. The response of channels along the grooves to the magnetic field orientation and the pronounced non-local transport strongly support a scenario of chiral boundary states in the 3D Landau band structure in the quantum limit. Specifically, the high-field conductance increases as trenches are added one by one, with the increase being proportional to the depth of the trenches. No strict quantization is detected or expected owing to the gapless bulk and the resulting finite lifetime of the chiral carriers. In addition, current flow along the edges of these channels are detected even between far-away contacts, a non-local signature at odds with a local conduction picture. These results demonstrate how chiral currents in the 3D quantum limit can be distributed across multiple designed etches, a shape-engineering freedom absent in the 2D world.

Results

The studied samples consist of rectilinear bars carved by FIB machining from a bismuth single crystal (Fig. 2). The details of the fabrication, particularly the great care taken to avoid any residual thermal mismatch strain by membrane suspending the bismuth structures, are detailed in Methods. As FIB machining is a maskless, direct-write technique, such

https://doi.org/10.1038/s41567-025-03146-7

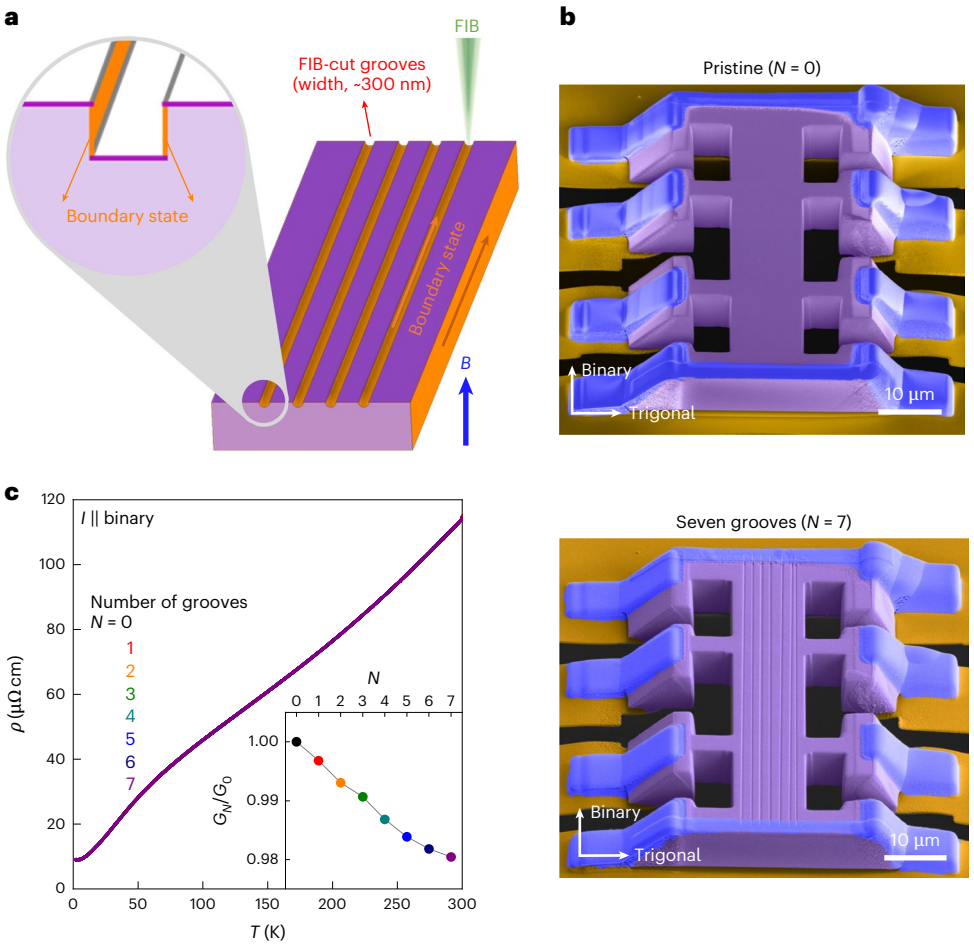

Fig. 2 | Seeding chiral boundary states via FIB-cut grooves. a, Schematic of chiral boundary states in a microstructured bismuth with FIB-cut grooves. Under strong magnetic fields driving the system into the quantum limit, bulk states are quantized, and chiral boundary states along the side surfaces parallel to the magnetic field dominate the charge conduction of the cuboid bismuth microstructure. By cutting grooves on the top surface with FIB, additional conduction paths are formed along the sidewalls of FIB-cut grooves. **b**, Scanning electron microscopy images of a microstructured bismuth before (top) and after (bottom) cutting seven grooves. **c**, Temperature-dependent electrical resistivity $\rho(T)$ of the microstructured bismuth with increasing number of grooves N on its surface. The inset shows the conductance of N-groove state G_N normalized by that of the pristine state G_0 at $T = 2$ K.

structures can be modified sequentially and the effect of the modifications is probed one by one. Here individual grooves of approximately 0.3 μm × 0.3 μm cross-section are added to the device to iteratively track the transport response to such surface modifications. Without magnetic fields, the conduction of our devices is mainly governed by the bulk conductance, as expected. The temperature-dependent resistivity $\rho(T)$ agrees well with measurements on the bulk bismuth crystal, with excess scattering from finite-size effects (Supplementary Note 1). The comparatively low residual resistivity ratio of the parent crystal of around $\rho(300\,\mathrm{K})/\rho(2\,\mathrm{K}) \approx 27$ indicates a moderate crystalline quality of bismuth, which was chosen on purpose to reduce classical finite-size effects and bulk conduction, to focus on the influence of the surface on transport. Measurements with an increasing number of grooves along the channel up to $N = 7$ are overlaid, and barely any differences are notable over the entire range of temperatures ($T = 2$–300 K; Fig. 2c). This is not surprising given the minute modification amounting to a total loss of 2% of the material. On closer inspection, the conductance of the device with N grooves, G_N, decreases as a function of N up to 2% (Fig. 2c, inset), which matches the loss of material and, therefore, agrees with the expectation of removing bulk channels. These results are entirely compatible with dominant bulk conduction in a device at zero field, as expected for a semimetal.

Next, out-of-plane magnetic fields are applied to drive the material into the quantum limit and probe the evolution of conduction (Fig. 3). The magnetoresistance (MR) $R(B)$ is quadratic in B around zero field followed by strong, B-linear growth, which abruptly terminates at a clear kink at $B^* \approx 2.7$ T, above which a saturated, sublinear behaviour is observed (Supplementary Fig. 2). This field scale coincides with the quantum limit $B_{QL} \approx 2.5$ T of electron pockets at the L points in this field direction[21] obtained self-consistently from quantum oscillations (Supplementary Note 2). Although the bulk crystal and microsample behave similarly in the low-field regime, they strongly differ in the quantum limit: the MR in the bulk crystal continues to grow without anomalies, as expected for the well-known nearly compensated semimetal behaviour of bismuth (Supplementary Fig. 1)[21,26]. A simple bulk band picture (for example, a two-band model) cannot account for this behaviour over the entire field range (Supplementary Note 3). Therefore, this observation points to the sizable surface conduction in the quantum limit, which naturally is more dominant in the microscopic bar. The link to the quantum limit strongly suggests that chiral boundary states play an important role, a connection that can be further substantiated by experiments.

The evolution of MR when adding grooves provides such a test for surface conduction. Indeed, the MR monotonically decreases as a function of N, which is prominent in high magnetic fields above B^* (Fig. 3a). For example, at $B = 14$ T, the resistance decreases from $R \approx 80\,\Omega$ of the pristine ($N = 0$) sample to $R \approx 74\,\Omega$ of the seven-groove ($N = 7$) sample, a reduction of approximately 7.5% (Fig. 3a, inset). Such a stronger effect

https://doi.org/10.1038/s41567-025-03146-7

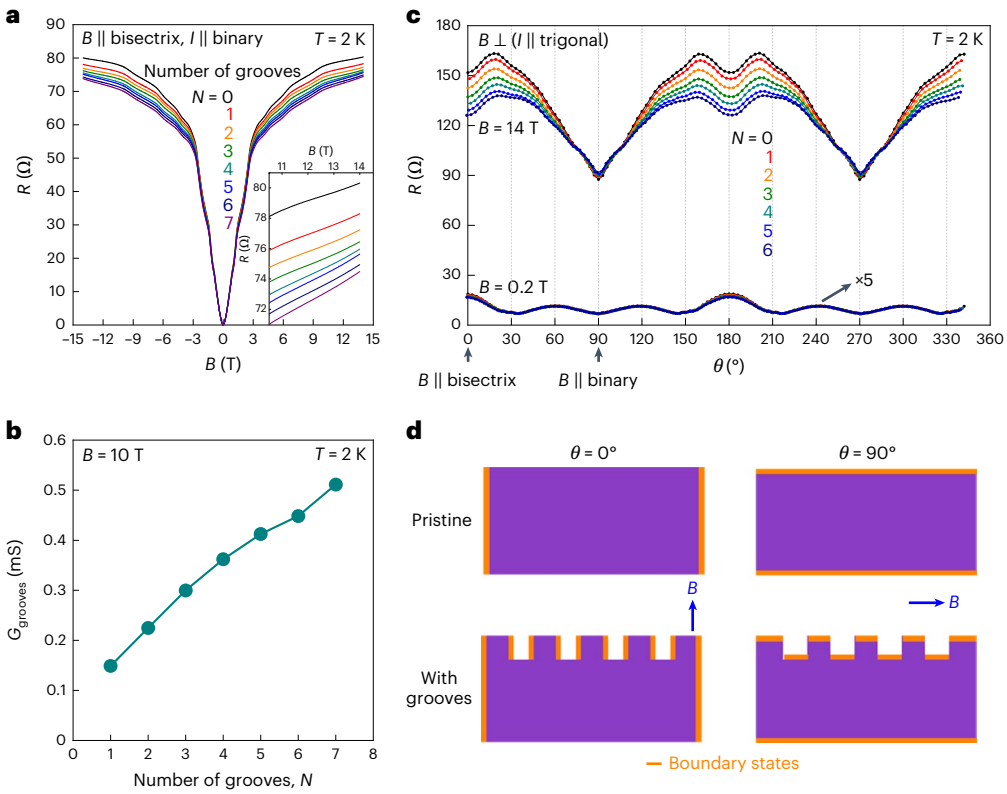

Fig. 3 | Magnetotransport of FIB-cut grooves. a, Magnetic-field-dependent electrical resistance $R(B)$ of the N-groove state with B || bisectrix and I || binary at $T = 2$ K. The inset shows $R(B)$ in high magnetic fields ($B > 10$ T). **b**, Conductance of grooves $G_{grooves}$ as a function of N with a magnetic field of 10 T at 2 K. The parallel-conductor model is used in estimating $G_{grooves}$ (Methods). **c**, Angle-dependent electrical resistance $R(\theta)$ of the N-groove state, where the magnetic field B (0.2 T, 14 T) is rotating in the plane perpendicular to the current direction (I || trigonal) at $T = 2$ K. **d**, Schematic of the chiral boundary states in the microstructured bismuth with different field angles. When the system is in the quantum limit, chiral boundary states (highlighted with the orange area) along sidewalls parallel to the magnetic field dominate the surface conduction. Cutting grooves effectively increases the surface area of the chiral boundary states under the out-of-plane magnetic field ($\theta = 0°$) but make negligible change with the in-plane magnetic fields ($\theta = 90°$).

of the grooves is opposite to the zero-field behaviour, as adding grooves increases the conductance above the quantum limit despite the reduction in the cross-sectional area (Fig. 3b). All these experiments are well reproduced in four bismuth microstructures despite a distinct variance in the groove depth and width (Supplementary Note 4), strengthening the evidence for conduction channels along the grooves. The additional surface conduction along the grooves reduces current flowing through the bulk, thereby consistently decreasing the Hall voltage of the device (Supplementary Fig. 5). As the grooves are connected between the current contacts bypassing the voltage contacts, they have an indirect and subdominant effect on the Hall voltage compared with the sidewalls of a rectilinear bar (Supplementary Note 5). We note that this experiment has no analogy in two dimensions as the number of edge modes in a 2D system is given by the Landau level index alone, regardless of the sample geometry. Thus, it is impossible to address the debate about whether currents run on the edge or in the bulk in the 2D QHE by similar geometric sample designs[1].

A further test of the chiral surface states involves the MR dependence on the field angle (Fig. 3c,d). It is yet another unique feature of 3D mesostructures in the quantum limit, as 2D QHE is purely driven by orbital effects that only depend on the scalar projection of the magnetic field onto the plane. In three dimensions, the field direction's role is much richer as it sets the quantization direction for the Landau levels with respect to the surfaces. At low fields below the quantum limit ($B = 0.2$ T), the angle-dependent MR $R(\theta)$ of the bars shows a 60° periodicity, reflecting the three-fold rotational symmetry of the crystal lattice and the bulk electronic system (with a weak two-fold component from classical ballistics; Supplementary Note 2)[27–29]. On the other hand, $R(\theta)$ in the quantum limit ($B = 14$ T) exhibits a strong two-fold symmetric response, which clearly reflects the sample shape instead of the lattice symmetry. The minimal value of the resistance is found for fields parallel to the long sideface of the bar ($\theta = 90°$), which corresponds to the larger surface of the rectangular bars. A shallower local minimum replaces the maximum MR in low fields at $\theta = 0°$, when the field is along the short face. We conclude that the excess conductivity is not an intrinsic property of the bar, but selectively arises in those sidewalls parallel to the magnetic field, which is where the chiral edge currents are located.

This point is further strengthened when the grooved samples are considered. The grooves cause a substantial difference in the angle-dependent MR. Under an out-of-plane magnetic field of 14 T ($\theta = 0°$), MR of the device with $N = 6$ grooves decreases almost 15% from the pristine state, in stark contrast to the negligible change observed at $\theta = 90°$. An explanation is found when considering the projected surface area. Although for $\theta = 0°$, the effective sidewall area is increased by the grooves, their net effect on the surface area for $\theta = 90°$ is zero (Fig. 3d). The field selectivity of the conductive surface further speaks against inadvertent surface modifications from FIB fabrication. Indeed, Xe-based machining of an elemental metal yields high-quality surfaces without compositional disorder and a sharply terminated single-crystal surface covered by few nanometres of nanocrystallite bismuth (Supplementary Note 6 provides an in-depth surface analysis via scanning transmission electron microscopy). The intrinsic nature of the chiral edge conductance in the quantum limit further reflects in reports of parallel-field-enhanced transport in macroscopic bismuth single crystals on the millimetre scale, where a substantial contribution of surface currents to the transport depends on the shape of the crystal[29].

https://doi.org/10.1038/s41567-025-03146-7

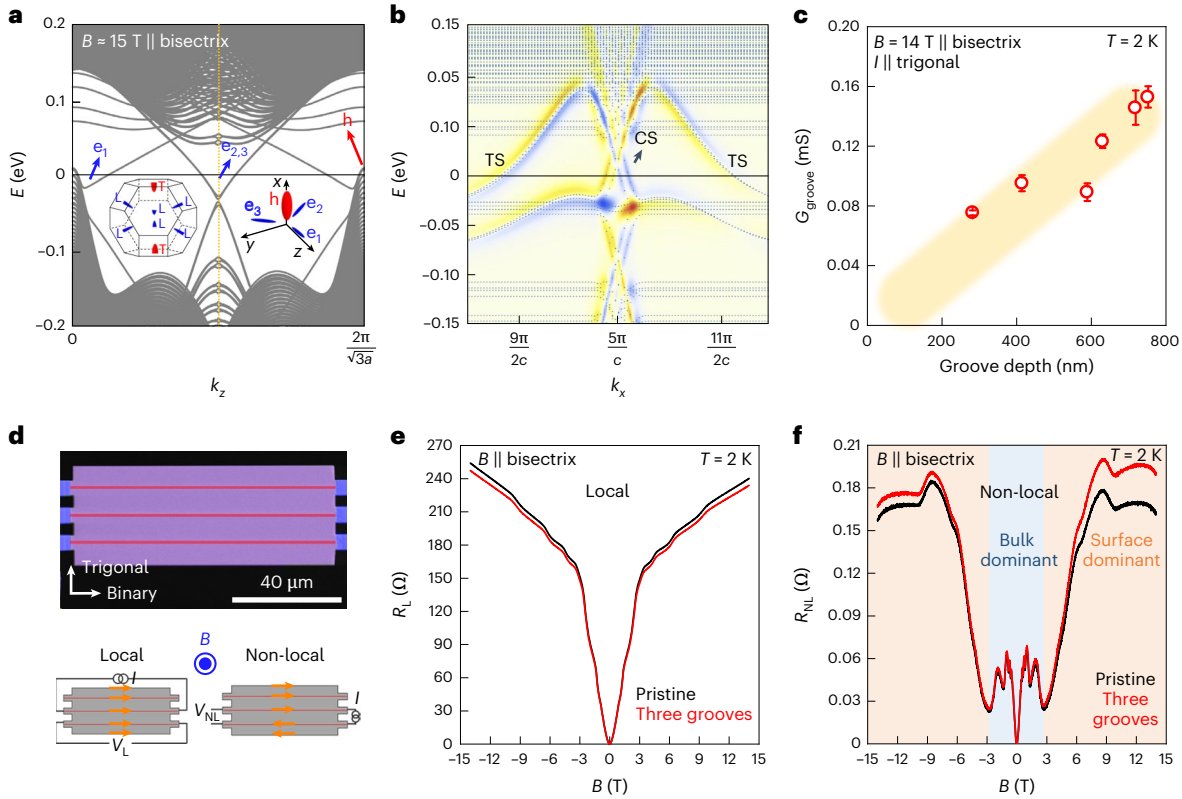

Fig. 4 | Non-local magnetotransport of FIB-cut grooves. a, Landau band structure of bismuth when a magnetic field $B \approx 15$ T is applied along the bisectrix axis ($N_y = 1{,}500$). The magnetic field is strong enough for all electron pockets at the L point from different valleys (e_1–e_3) to be in the quantum limit, except the hole pocket (h) at the T point. The dashed orange line indicates the k_z momentum for the surface spectral density in **b**. The insets depict the sketch of the Brillouin zone and Fermi surfaces of bismuth. **b**, Surface spectral density for $B \approx 15$ T for a slab thickness of $N_y = 1{,}500$ unit cells. The localized states on opposite sidewalls are differentiated by yellow and blue. The chiral surface states (CS) manifest an imbalance between right- and left-moving modes on each surface, whereas the trivial surface states (TS) come in pairs of right and left movers per surface. **c**, Conductance of individual groove G_{groove} as a function of groove depth, with $B = 14$ T along the bisectrix at $T = 2$ K. The error bars represent the variation obtained by averaging two longitudinal voltage pairs of the Hall-bar structure. **d**, Scanning electron microscopy image of a non-local geometry device, after cutting three grooves (red lines) between each longitudinal electrodes pair (top). Bottom: schematics of the local (left) and non-local configurations (right) of current and voltage electrodes. The effective current paths via chiral boundary states in the device are highlighted as arrows. **e**,**f**, Magnetic-field-dependent local resistance R_L (**e**) and non-local R_{NL} (**f**) at $T = 2$ K, where $R_{L(NL)} = V_{L(NL)}/I$, before (black) and after (red) cutting three grooves.

The experimental observations unequivocally demonstrate substantial charge transport carried by chiral edge currents, which naturally arise from microscopic modelling in tight-binding calculations (Methods). The calculated Landau band structure of bismuth captures the experimental situation with the electron pockets at the L points from three valleys being in the quantum limit, and a hole pocket at the T point that is not (Fig. 4a). Here the occupied momentum range of k_z at the lowest Landau band contributes to chiral boundary states, which is highlighted in the (side) surface spectral function (Fig. 4b). In this picture, the number of surface modes contributing to transport should scale with the groove depth, though the effect of hybridization between modes and confinement for shallow grooves (less than 300 nm deep) may lead to small modifications from a linear relation. The linear relation is indeed confirmed by varying the depth of the grooves within the same device and estimating the conductance of each groove, denoted as G_{groove} (Fig. 4c and Supplementary Note 4).

A different possible origin of the excess conductance observed in our experiments may be regular surface states, especially well known to be metallic and abundant in bismuth[30]. Indeed, our calculations consistently yield surface states corresponding to large Fermi surfaces (Supplementary Fig. 7). However, they are difficult to reconcile with an enhancement in sidewall conductivity that follows the direction of the magnetic field. The size of the Fermi surface implies that the surface is far from the quantum limit under laboratory fields; hence, a semiclassical description is applicable. In this surface-state scenario, the semiclassical surface may either be in a clean limit $\omega_c\tau \gg 1$ or dirty limit $\omega_c\tau \ll 1$ (ω_c is the cyclotron frequency and τ is the relaxation time). Within the diffusion picture of the dirty limit, magnetic fields have a negligible effect on transport from a Kohler scaling argument, contrary to the experimental observation. This leaves only a surface state in the clean limit, in which the magnetic field ought to completely suppress the conductance in surfaces normal to the field. Hence, carriers in perpendicular fields would be localized, whereas sidewalls under parallel fields remain highly conductive due to the lack of orbital effects. This scenario is also at odds with our observations. First, the zero-field resistivity increases when adding grooves, despite the growing surface-to-bulk ratio. Further, these surface states do not appear as Shubnikov–de Haas oscillations despite the need for them to be in the clean limit. Last, a clean-limit surface is difficult to reconcile with the nanocrystalline, disordered nature of the FIB-irradiated surface. In particular, naturally introduced nanometric roughness on the sidewall, due to ion-beam interactions that depend on the crystallographic orientation of bismuth (Supplementary Note 7), should strongly suppress conduction via trivial surface states; however, our observation shows that surface conduction remains robust against such roughness. This is consistent with the chiral-boundary-state scenario, as they remain unimpeded by such surface disorder akin to the robust nature of the 2D QHE edges.

A further direct test for chiral boundary states is the strong non-locality of transport emerging in the quantum limit. In quantum Hall states, quantum spin Hall states and topological insulators, non-locality has been a key observable to demonstrate their non-trivial charge flow[31–36]. To this end, we probe a rectangular microstructure with six electrodes, three close-by ones on each side (5-μm spacing) separated by a 96-μm-long block of bismuth (Fig. 4d). In this geometry, we can first probe the local resistance $R_L = V_L/I$, which arises from currents flowing across the whole microstructure. This can be compared with the non-local resistance $R_{NL} = V_{NL}/I$, where currents flow within one side of the microstructure and non-local signals are received between voltage electrodes on the opposite side. The ohmic contribution to the non-local voltages at distance L given the local spacing of electrodes w is suppressed by a factor $\exp(-\pi L/w)$ when $L \gg w$ (refs. 36,37). The zero-field voltage measured in the non-local configuration is consistently observed to be reduced by a factor of 100 compared with the local current configuration ($R_{NL} \approx 0.01 R_L$). Connecting these far-away electrodes by grooves should enhance non-locality and increase the far-away voltage signals above the ohmic limit given they host chiral conductive states. This is indeed observed experimentally.

At zero field, no change to the non-local signal from added grooves is observed, as expected from the negligible change in shape, further excluding the addition of a trivial conductive layer. Below the quantum limit, $R_{NL}(B)$ exhibits substantially enhanced quantum oscillations, reflecting the sensitivity of charge injection to Landau quantization. As the material enters the quantum limit, $R_{NL}(B)$ steeply rises. In particular, this rise begins only beyond the kink of the local MR at $B^* \approx 2.7$ T. Evidently, the current distribution substantially changes in the quantum limit, and the sublinearity of R_{NL}(B) in high fields is associated with substantial surface currents. Although $R_L(B)$ increases by 32% from 6 T to 14 T, $R_{NL}(B)$ remains at a saturated value in the high-field region. Such behaviour is naturally expected from chiral boundary states, which, once formed in the quantum limit, exhibit no further field dependence.

Outlook

Our results highlight the importance of chiral boundary states in gapless 3D metals in the quantum limit. The natural absence of quantization in such gapless systems may mislead one to underestimate their role in conduction. Their long lifetime remains finite due to finite scattering matrix elements to the gapless bulk, with similarities to the situation in the quantum spin Hall effect. First, our results provide a viewpoint on the importance of surface phenomena in interpreting signatures of strongly correlated physics in the 3D quantum limit studied by transport, such as the valley-polarized high-field state of bismuth or the cascade of field-induced phase transitions in the quantum limit of graphite[21,38,39]. Compatible observations of excess conductance on surfaces parallel to the magnetic field suggest that such physics may well influence—if not dominate—the quantum-limit transport of macroscopic crystals at high purity. Second, the much richer design space of boundaries of 3D objects will provide a versatile platform to tune and design response functions in the quantum limit, with non-trivial tuning via the magnetic field direction. Surface shapes with rotational symmetries differing from the crystalline symmetries and the direct writing of chiral channels are natural directions to explore such physics in the 3D quantum limit. Next to the investigations of gapped and quantized topological phases of matter, it appears the physics of gapless quantum-limit metals deserves closer attention, too.

Online content

Any methods, additional references, Nature Portfolio reporting summaries, source data, extended data, supplementary information, acknowledgements, peer review information; details of author contributions and competing interests; and statements of data and code availability are available at https://doi.org/10.1038/s41567-025-03146-7.

References

1. Klitzing, K. V., Dorda, G. & Pepper, M. New method for high-accuracy determination of the fine-structure constant based on quantized Hall resistance. *Phys. Rev. Lett.* **45**, 494–497 (1980).
2. Thouless, D. J., Kohmoto, M., Nightingale, M. P. & den Nijs, M. Quantized Hall conductance in a two-dimensional periodic potential. *Phys. Rev. Lett.* **49**, 405–408 (1982).
3. Niu, Q., Thouless, D. J. & Wu, Y.-S. Quantized Hall conductance as a topological invariant. *Phys. Rev. B* **31**, 3372–3377 (1985).
4. Chu, R.-L., Shi, J. & Shen, S.-Q. Surface edge state and half-quantized Hall conductance in topological insulators. *Phys. Rev. B* **84**, 085312 (2011).
5. Wang, C. M., Sun, H.-P., Lu, H.-Z. & Xie, X. C. 3D quantum Hall effect of Fermi arcs in topological semimetals. *Phys. Rev. Lett.* **119**, 136806 (2017).
6. Yan, B. & Felser, C. Topological materials: Weyl semimetals. *Annu. Rev. Condens. Matter Phys.* **8**, 337–354 (2017).
7. Burkov, A. Weyl metals. *Annu. Rev. Condens. Matter Phys.* **9**, 359–378 (2018).
8. Armitage, N. P., Mele, E. J. & Vishwanath, A. Weyl and Dirac semimetals in three-dimensional solids. *Rev. Mod. Phys.* **90**, 015001 (2018).
9. Halperin, B. I. Possible states for a three-dimensional electron gas in a strong magnetic field. *Jpn. J. Appl. Phys.* **26**, 1913–1919 (1987).
10. Störmer, H. L., Eisenstein, J. P., Gossard, A. C., Wiegmann, W. & Baldwin, K. Quantization of the Hall effect in an anisotropic three-dimensional electronic system. *Phys. Rev. Lett.* **56**, 85–88 (1986).
11. Montambaux, G. & Kohmoto, M. Quantized Hall effect in three dimensions. *Phys. Rev. B* **41**, 11417–11421 (1990).
12. Kohmoto, M., Halperin, B. I. & Wu, Y.-S. Diophantine equation for the three-dimensional quantum Hall effect. *Phys. Rev. B* **45**, 13488 (1992).
13. Bernevig, B. A., Hughes, T. L., Raghu, S. & Arovas, D. P. Theory of the three-dimensional quantum Hall effect in graphite. *Phys. Rev. Lett.* **99**, 146804 (2007).
14. Tang, F. et al. Three-dimensional quantum Hall effect and metal-insulator transition in $ZrTe_5$. *Nature* **569**, 537–541 (2019).
15. Qin, F. et al. Theory for the charge-density-wave mechanism of 3D quantum Hall effect. *Phys. Rev. Lett.* **125**, 206601 (2020).
16. Galeski, S. et al. Origin of the quasi-quantized Hall effect in $ZrTe_5$. *Nat. Commun.* **12**, 3197 (2021).
17. Uchida, M. et al. Quantum Hall states observed in thin films of Dirac semimetal Cd_3As_2. *Nat. Commun.* **8**, 2274 (2017).
18. Schumann, T. et al. Observation of the quantum Hall effect in confined films of the three-dimensional Dirac semimetal Cd_3As_2. *Phys. Rev. Lett.* **120**, 016801 (2018).
19. Zhang, C. et al. Quantum Hall effect based on Weyl orbits in Cd_3As_2. *Nature* **565**, 331–336 (2019).
20. de Haas, W. J. & van Alphen, P. M. The dependence of the susceptibility of diamagnetic metals upon the field. *Proc. Netherlands Roy. Acad. Sci* **33**, 1106–1118 (1930).
21. Zhu, Z., Fauqué, B., Behnia, K. & Fuseya, Y. Magnetoresistance and valley degree of freedom in bulk bismuth. *J. Phys. Condens. Mater* **30**, 313001 (2018).
22. Drozdov, I. K. et al. One-dimensional topological edge states of bismuth bilayers. *Nat. Phys.* **10**, 664–669 (2014).
23. Murani, A. et al. Ballistic edge states in bismuth nanowires revealed by SQUID interferometry. *Nat. Commun.* **8**, 15941 (2017).
24. Schindler, F. et al. Higher-order topology in bismuth. *Nat. Phys.* **14**, 918–924 (2018).
25. Bernard, A. et al. Long-lived Andreev states as evidence for protected hinge modes in a bismuth nanoring Josephson junction. *Nat. Phys.* **19**, 358–364 (2023).

26. Sáenz-Hernández, A. et al. Cryogenic focused ion beam milling to investigate the anisotropic magnetotransport properties of bismuth microcrystals. *Adv. Funct. Mater.* e17475 (2025).
27. Zhu, Z., Collaudin, A., Fauqué, B., Kang, W. & Behnia, K. Field-induced polarization of Dirac valleys in bismuth. *Nat. Phys.* **8**, 89–94 (2012).
28. Collaudin, A., Fauqué, B., Fuseya, Y., Kang, W. & Behnia, K. Angle dependence of the orbital magnetoresistance in bismuth. *Phys. Rev. X* **5**, 021022 (2015).
29. Kang, W., Spathelf, F., Fauqué, B., Fuseya, Y. & Behnia, K. Boundary conductance in macroscopic bismuth crystals. *Nat. Commun.* **13**, 189 (2022).
30. Hofmann, P. The surfaces of bismuth: structural and electronic properties. *Prog. Surf. Sci.* **81**, 191–245 (2006).
31. Roth, A. et al. Nonlocal transport in the quantum spin Hall state. *Science* **325**, 294–297 (2009).
32. Brüne, C. et al. Spin polarization of the quantum spin Hall edge states. *Nat. Phys.* **8**, 485–490 (2012).
33. McEuen, P. L. et al. New resistivity for high-mobility quantum Hall conductors. *Phys. Rev. Lett.* **64**, 2062–2065 (1990).
34. Haug, R. J. Edge-state transport and its experimental consequences in high magnetic fields. *Semicond. Sci. Technol.* **8**, 131 (1993).
35. Xu, Y., Miotkowski, I. & Chen, Y. P. Quantum transport of two-species Dirac fermions in dual-gated three-dimensional topological insulators. *Nat. Commun.* **7**, 11434 (2016).
36. Abanin, D. A. et al. Giant nonlocality near the dirac point in graphene. *Science* **332**, 328–330 (2011).
37. van der Pauw, L. J. A method of measuring the resistivity and Hall coefficient on lamellae of arbitrary shape. *Philips Tech. Rev.* **20**, 220 (1958).
38. Zhu, Z. et al. Emptying Dirac valleys in bismuth using high magnetic fields. *Nat. Commun.* **8**, 15297 (2017).
39. Yaguchi, H. & Singleton, J. A high-magnetic-field-induced density-wave state in graphite. *J. Phys. Condens. Mater* **21**, 344207 (2009).

Methods

Membrane-based microstructuring

Single crystals of bismuth were commercially obtained from MaTecK. For microstructuring, we adopted a membrane-based microstructuring technique[40] to avoid residual thermal mismatch strain. Lamellae were cut from a single crystal of bismuth using a Xe-plasma FIB system. To achieve a smoothly polished surface on the lamella, a protection layer was deposited in situ by Pt deposition with the assistance of an electron beam, followed by FIB-assisted deposition. Trenches on both sides of the lamella were cut using Xe FIB with an acceleration voltage of 30 kV and a current of 60 nA (Xe, 30 kV, 60 nA). Final polishing under grazing incidence was performed by Xe (30 kV, 1 nA). The lamella was then transferred to a gold-coated SiN_x membrane (50-nm-thick SiN_x, 10/150-nm-thick Ti/Au) in situ by a micromanipulator. FIB-assisted Pt deposition was used to establish electrical contacts between the lamella and the gold layer. All electrodes were then separated by cutting the gold-coated SiN_x membrane by Xe (30 kV, 1 nA). Additionally, all gold-coated SiN_x membranes connected to the electrodes were cut into springs to release strain. Before final patterning, the top surface was exposed to Xe (8 kV, 0.1 nA) to remove overspray from the Pt deposition process. Finally, the lamella was patterned into the desired shape with Xe (30 kV, 1 nA). Grooves were cut with Xe (30 kV, 3 pA) with a typical dose of 100–200 pC μm^{-2}.

Parallel-conductor model

We consider conduction channels along the grooves as parallel conductors isolated from the rest bulk and surface to quantify the conductance of conduction channels. In this model, the applied electric current I_{total} is divided into grooves ($I_{grooves}$) and the rest bulk and surface ($I_{pristine}$), and their ratio is decided by their conductance $G_{grooves}$ and $G_{pristine}$. From this model, we can estimate the conductance of grooves as $G_{grooves} = G_{pristine}I_{grooves}/I_{pristine} = G_{pristine}(I_{total} - I_{pristine})/I_{pristine} = G_{pristine}(I_{total}/I_{pristine} - 1)$. We first look at $I_{pristine}$. If we neglect the effect of the removed portion of bismuth by cutting grooves (indeed negligible, as shown in Fig. 2c), the measured $R = V_{xx}/I_{total}$ should be the same for every N. Hence, for $N \geq 1$, we can get $I_{pristine}$ from the relation $V_{xx}(N = 0)/I_{total} = V_{xx}(N)/I_{pristine}$. Second, we focus on $G_{pristine}$. Since we measured R of the microstructure with the four-probe method, we should scale this to $R_{pristine}$, which is the resistance of the entire length of the microstructure between the current electrodes, where the grooves are also connected. From the relation $R = \rho l/A$ (ρ is the resistivity and l (A) is the length (cross-sectional area) of a microstructure), we take $R_{pristine} = RL/L_{4p}$, where L and L_{4p} are distances between the current and voltage electrodes in a Hall-bar structure, respectively. Afterwards, we get $G_{pristine} = 1/R_{pristine}$ by neglecting the Hall effect contribution for simplicity, and take this value for every N to calculate $G_{grooves}$.

Tight-binding calculation

We model the electronic structure of bismuth in a tight-binding approximation using the model introduced in ref. 41, including the notation of lattice parameters a and c, as well as primitive lattice vectors $\mathbf{a}_i$, $i = 1, 2, 3$ (Supplementary Fig. 9). Our objective is to model the surface states on the sidewalls of the groove. Such states may have two origins: (1) bismuth has (non-topological) surface states and (2) in a magnetic field, chiral boundary modes connecting bulk Landau levels emerge.

We chose the Cartesian coordinates to align with the crystallographic axes as follows: binary, y axis; bisectrix, z axis; trigonal, x axis. The magnetic field is applied parallel to the bisectrix—the z axis—and the surface normal we consider is the binary, meaning the y axis. We choose a gauge, in which both surface momenta k_x and k_z are good quantum numbers. For this slab calculation, the unit cell needs to be doubled (compared with the primitive one) and we introduce the new lattice vectors $\mathbf{e}_1 = \mathbf{a}_2 - \mathbf{a}_1$, $\mathbf{e}_2 = \mathbf{a}_1 + \mathbf{a}_2 + \mathbf{a}_3$, $\mathbf{e}_3 = \mathbf{a}_3$. Note that $\mathbf{e}_1$ and $\mathbf{e}_2$ are pointing in the binary and trigonal directions, respectively. The slab thickness in units of $|\mathbf{e}_1|$ is reported as N_y. The magnetic field enters both as a Zeeman field and through orbital coupling via Peierl's substitution. For the former, we use a g factor of $g = 20$, representing an average of the valley-specific and anisotropic g-tensor reported for bismuth (since we are interested in a field range of up to 20 T only, this approximation is sufficient). Note that the smallest non-zero magnetic field in the bisectrix direction that can be accommodated in a system with periodic boundary conditions in all directions—this corresponds to a cluster of $N_y \times 1 \times 1$ unit cells in the $\mathbf{e}_1$, $\mathbf{e}_2$ and $\mathbf{e}_3$ directions—is given by

$$B = \frac{6\pi}{caN_y}\frac{\phi_0}{2\pi} \approx \frac{23,000\,\mathrm{T}}{N_y}, \quad (1)$$

where $\phi_0 = h/e$, and c and a are the lattice constants of bismuth. For a realistic field of $B \approx 15$ T, we, thus, need a slab width of $N_y = 1{,}500$. Given a lattice constant in this direction of $a = 4.5$ Å, this would correspond to a thickness of $w \approx 0.7$ µm.

With this tight-binding model, we numerically solve for the energy spectrum $\epsilon_{\mathbf{k},\alpha}$ and eigenstates $|\mathbf{k}, \alpha\rangle$, where α labels all other degrees of freedom except momentum ($\mathbf{k} = (k_x, k_z)$). The surface spectral function is given by states

$$A(\mathbf{k}, \omega) = \frac{1}{\pi}\mathrm{Im}\{\mathrm{Tr}[G(\mathbf{k}, \omega - i\eta)\hat{P}_{surf}]\}, \quad (2)$$

where $\hat{P}_{surf}$ projects states onto the unit cells on the surface of the slab and η is a regularization set to 10 meV.

Figure 4a shows the Landau level spectrum for periodic boundary conditions and a magnetic field $B \approx 15$ T. As mentioned above, to include a magnetic field of this size, we need $N_y = 1{,}500$. For this field, the electron-like L pockets are in the quantum limit with the zeroth, non-spin degenerate Landau level below the Fermi energy[21], whereas the hole-like T pocket has its top three Landau levels occupied (with spin near-degeneracy), totalling to six Landau bands above the Fermi level.

We calculate the surface spectral function for the same parameters for open-boundary conditions (Fig. 4b), clearly featuring the chiral boundary states around the L point (the full spectral function along this k_z cut is shown in Supplementary Fig. 7b). For comparison, Supplementary Fig. 7a shows the same cut without a magnetic field, with the inset showing the surface Fermi surface structure. We observe extensive Fermi contours spanning the entire surface Brillouin zone. Note that in this geometry, one of the three L points and the T point project to the same surface momentum, and the other two L points project to another surface momentum, as indicated.

Data availability

The data that support the findings of this study are available via Figshare at https://doi.org/10.6084/m9.figshare.30428701.v1. Source data are provided with this paper.

References

40. Guo, C. et al. Switchable chiral transport in charge-ordered kagome metal CsV_3Sb_5. *Nature* **611**, 461–466 (2022).
41. Liu, Y. & Allen, R. E. Electronic structure of the semimetals Bi and Sb. *Phys. Rev. B* **52**, 1566–1577 (1995).

Acknowledgements

This work was funded by the European Union under the Horizon Europe research and innovation programme (ERC Consolidator Grant, XBEND—grant agreement number 101080740). C.M.G. was funded by the European Research Council (ERC) under grant Free-Kagome (grant agreement number 101164280). B.H.G. was supported by the Schmidt Science Fellows in partnership with the Rhodes Trust, and by the Max Planck Society. T.N. acknowledges support from the Swiss National Science Foundation through a Consolidator Grant (iTQC, TMCG-2_213805) and a Quantum grant (20QU-1_225225).

Author contributions

J.S., C.M.G., C.P., X.H. and P.J.W.M. performed the experiment design, FIB microstructuring and magnetotransport measurements. Y.C.W., M.H.F. and T.N. developed the general theoretical framework and performed the tight-binding calculations. B.H.G. performed the scanning transmission electron microscopy and analysed the surface atomic structure. All authors were involved in writing the paper.

Funding

Open access funding provided by Max Planck Society.

Competing interests

The authors declare no competing interests.

Additional information

Supplementary information The online version contains supplementary material available at https://doi.org/10.1038/s41567-025-03146-7.

Correspondence and requests for materials should be addressed to Junho Seo, Mark H. Fischer, Titus Neupert or Philip J. W. Moll.

Peer review information *Nature Physics* thanks Gregor Hlawacek and the other, anonymous, reviewer(s) for their contribution to the peer review of this work.